Formation of Chain-Folded Structures in Supercooled Polymer Melts Examined by MD Simulations

Hendrik Meyer*,† and Florian Müller-Plathe‡

Institut Charles Sadron, C.N.R.S., 6, rue Boussingault, 67083 Strasbourg, France, and Max-Planck-Institut für Polymerforschung, 55021 Mainz, Germany

Received July 23, 2001; Revised Manuscript Received November 16, 2001

ABSTRACT: We report the first computer experiments with supercooled polymer melts of chains long enough to form chain-folded structures. These structures resemble the lamellae of polymer crystals, and the inverse of the lamellar thickness is related linearly to the crystallization temperature as found in experiments. The small- and wide-angle scattering intensities start growing at about the same time. However, the wide-angle scattering signal is very weak at the beginning. We use molecular dynamics (MD) simulations with a coarse-grained polymer model for chain lengths of $N = 100$ monomers. The model consists of spherical beads connected by harmonic springs with an additional angle bending potential reflecting the torsional states of the underlying atomistic backbone. It demonstrates that chain stiffness alone without an attractive interparticle potential is a sufficient driving force for the formation of chain-folded structures. We discuss the evolution of structure in the homogeneous nucleation regime as well as the melting process. The influence of the finite size accessible in direct MD simulation of polymer crystallization is discussed critically.

1. Introduction

Since the publication of the idea of chain-folded lamellae in polymer crystallization,[1−3] the discussion about the crystallization process is still going on both experimentally and theoretically.[4−15] Especially the early stage of crystal formation has recently attracted much interest since experiments found that the small-angle scattering intensity increases before the appearance of wide-angle Bragg peaks. The large-scale structure formation related to the SAXS signal has been interpreted as a spinodal mode.[11,16−18] The possibility of spinodal-assisted crystallization has also been formulated theoretically in a model using density and orientational order parameters.[10] The lamellae of polymer crystals are probably nonequilibrium structures, and Keller and co-workers discussed the role of metastability.[4,19] These and other results lead Strobl to propose a new scenario for polymer crystallization in the melt.[6] The process should start with a mesomorphic phase leading to small crystalline blocks which finally merge in a rather collective process to form the crystal lamellae. The generality of this (still qualitative) picture was immediately questioned by the counterexample of polymers as isotactic polypropylene crystallizing as helices of a certain chirality. The necessity of selecting the chirality of the chains makes a collective merging of the final crystal structure very improbable.[7]

One difficulty to advance the understanding of the polymer crystallization process is that experimental insight is rather indirect. Scattering experiments always give quantities averaged over the whole sample. AFM techniques recently gave some new insight and were even able to observe the growth and melting of single lamellae in real time.[20,21] However, it is still impossible to resolve the dynamics of single polymer chains during the crystallization process. This is the point where computer modeling may give complementary information since molecular dynamics simulations provide the trajectory of all individual particles. However, because of finite computer resources, model simulations can only cover partial aspects, too.

Much effort has already been spent on modeling polymer crystallization by means of computer simulations. The thickness selection in polymer crystals was modeled by Monte Carlo methods on a lattice[22−25] as well as by molecular dynamics (MD) on a predefined crystal front.[26] All these studies rely on the hypothesis of a growth front separating the crystalline phase from the amorphous melt. The Sadler−Gilmer model[22] allows this surface to be less regular; however, the presence of neighboring lamellae or the possibility of further chain movement behind the growth front is usually not taken into account. Direct MD simulation of the structure formation was so far used for studying either short chains in the melt,[27] of a cluster in a vacuum,[28] or in thin films.[29] Using MD, the role of chain folding has been considered mainly in the collapse of an isolated long chain to a crystalline globule[30−33] as well as in a Langevin dynamics study of several chains in solution.[34]

This paper demonstrates that the simulation of the formation of chain-folded structures in supercooled polymer melts is possible. We analyze this process as well as the subsequent melting of these structures in detail. In the present study of long chains at melt densities, we try to make as few restrictions as possible and study the chain ordering from the homogeneous nucleation in a simulation cell with periodic boundary conditions. The influence of these boundary conditions will be discussed. No condition on the initial nucleus and no lattice is involved. Preliminary results of this study have recently been reported.[35] The present paper focuses on the results obtained with long chains of $N = 100$ monomers. Aspects of structure formation of short chains and chain length dependence will be published elsewhere.[36]

† Laboratoire Européen Associé ICS, MPI-P.
‡ MPI-P.
* Corresponding author.

10.1021/ma011309l CCC: $22.00
Published on Web 01/19/2002

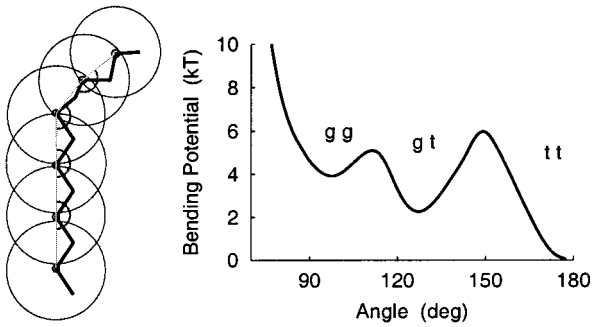

Figure 1. Sketch of the coarse-grained model "CG-PVA". Each bead represents a monomer with two carbon atoms on the backbone. Successive beads are connected by harmonic springs. Three successive beads interact via the shown angle bending potential. The minimum at 180° corresponds to two successive trans torsions on the atomistic backbone. The minima "gg" and "gt" correspond to gauche−gauche and gauche−trans sequences, respectively.

2. Computational Methods

2.1. The Model "CG-PVA". We use a simplified version of a model for poly(vinyl alcohol) (PVA) derived by a systematic coarse-graining procedure[37] from fully atomistic simulations. A coarse-grained bead represents one monomeric unit of PVA. The beads are connected by harmonic springs and, in addition, an angle bending potential containing information on the torsional states of the atomistic backbone. The angle bending potential was derived directly from the Boltzmann-inverted angle distribution of the atomistic trajectories. The nonbonded potential was optimized to fit the corresponding radial distribution function of the atomistic simulation. For the present study of polymer crystallization, we reduced the model to its essential ingredients which are the angle bending potential and the excluded-volume interaction. The latter is approximated by a Lennard-Jones 9−6 potential which is softer than the standard Lennard-Jones 12−6 potential. This is suitable at this level of coarse graining because one bead represents a whole monomer which is definitely softer than single atoms. Furthermore, for the simulation of a dense melt, it is sufficient to take only the repulsive part of the potential.[38] The attractive part of the potential is indirectly considered by the applied external pressure. This leads to some shift of energy and pressure while it affects only little the qualitative behavior of the system.

The parameters defining our model are given in the following. Length scales are fixed by the mapping from atomistic simulations. Units are reported in $\sigma = 0.52$ nm, corresponding roughly to the chain diameter of PVA. The bond length is $0.5\sigma = 0.26$ nm. In these units, the density is about 2.1 monomers per σ^3. The nonbonded potential between monomers is $V(r)/k_B = 0.53/r^9 - 0.75/r^6$, which is cut and shifted to zero at the minimum $r_{cut} = 1.02\sigma$. Nonbonded interactions between first and second neighbors along each chain are excluded. The angle potential shown in Figure 1 has three minima at 180°, 126°, and 95°, corresponding to trans−trans, trans−gauche, and gauche−gauche conformations of the atomistic backbone chain. There is no torsional potential and no charges. The equations of motion are integrated by the velocity-Verlet algorithm using a time step of 0.005τ, and the nonbonded forces are calculated with a linked cell algorithm.[39] Temperature is kept constant through a Langevin thermostat with friction constant $\Gamma = 0.5$. Temperatures and energies are expressed in dimensionless units with $m = k_B = 1$; $T = 1$ corresponds to the high-temperature phase of the amorphous melt. Constant pressure is imposed by the isotropic Berendsen manostat.[40] The simulations are performed in a cubic box with periodic boundary conditions. In some cases, the pressure was also controlled independently in the three dimensions (see section 3.4). Calculations have been performed on a cluster of Alpha EV6 and EV67 processors; the average time needed for one run of 120.000τ with 19 200 monomers is about 1 month.

2.2. Discussion of Approximations. The investigation of structure formation in supercooled polymer melts of long chains by direct MD simulations is a difficult task since one needs large systems and long simulation times to arrive at the lamellar-like structures of polymer crystals (2×10^4 to 10^5 monomers are simulated for about 3×10^7 integration steps per system). Two approximations make this work feasible:

(i) A bead−spring model with one bead representing a whole monomer is used. For PVA, this reduces the number of particles to simulate by a factor of 7 with respect to an all-atom model and still by a factor of 4 with respect to often used united-atom models where only the neighboring hydrogens are absorbed into the backbone carbons. By our coarse-graining procedure,[37] the atomistic torsions become bending angles of the coarse-grained model. Probably, it is difficult to coarse grain even further than our model, at least as long as one is still interested in local conformations as during the crystallization process. Because of this approximation, we lose the zigzag structure of the chains and the model chains have cylindrical symmetry. We thus expect them to order in a hexagonal lattice.

(ii) Only the repulsive part of the nonbonded potential is taken into account. This speeds up the simulation since the cutoff radius of the nonbonded interactions determines crucially the number of pairs which have to be considered in each integration step. Moreover, this second approximation may yield interesting implications for possible new theories of polymer crystallization. It also switches off one possible driving force of crystallization, the cohesive energy, which would increase with decreasing temperature. Thus, when lowering the temperature, only the chain stiffness will increase in our model. It is well-known that crystallization happens also in purely repulsive systems of small molecules as hard spheres or liquid crystals. It is interesting to note that the chain-folded structures of polymer crystals can also be obtained without explicit attraction between the monomers. In this sense, our model may perhaps be viewed as a realization of the intermediate liquid-crystalline (LC) phase discussed by Olmsted et al.[10] as a hidden metastable phase in the phase diagram. Because of the two approximations, our model chains have little structure, and the real 3D crystal structure is suppressed, thus making the hidden LC phase visible. To avoid misunderstandings, we note that our chains have no intrinsically stiff parts and are still flexible—the notion LC is used in the sense that the structure formation is driven to a large extent by the parallel ordering of bonds. The chains have still some mobility along their contour. However, they are well confined to the hexagonal lattice—there is no lateral liquidlike mobility.

Though we started from atomistic simulations for PVA, the approximations make the resulting coarse-

Table 1. Systems Simulated of 192 CG-PVA 100-mers

T_c	time ($10^3\tau$)	T_{melt}	s^a
0.80	150	0.965	40
0.78	150	0.945	36
0.76	80	0.925	32
0.74	125	0.92	30
0.70	140	0.905	26
0.66	125	0.88	22

constant rate (τ^{-1})	time ($10^3\tau$)	T range
20×10^{-6}	25	1.0−0.5
5×10^{-6}	40	0.8−0.6
2×10^{-6}	100	0.8−0.6

[a] s = average stem length (in number of monomers) deduced from intrachain orientation correlation. The three cooling rates will be referred to as fast, intermediate, and slow.

grained model rather generic. It probably describes as well polyethylene (PE), especially because PE and PVA have the same monomer number density and a qualitatively similar angle bending potential. The main difference is the polar OH group on PVA, which is, however, only indirectly taken into account in our simulation.

3. Structure Formation in the Supercooled Melt

Two kinds of "experiments" have been performed: reducing temperature at a constant rate and isothermal relaxation after a sudden temperature quench. Table 1 gives an overview over the crystallization runs discussed in the following. They have been performed with 192 chains of length $N = 100$ in a cubic box. The start configuration was generated as random walks and equilibrated at $T = 1.0$ for 20 000τ. (The time autocorrelation function of the end-to-end vector decays to 0.2 during this time.) Simulations with different size have been performed to check finite size effects and will be discussed later.

3.1. Isothermal Relaxation. Figure 2 contains the evolution of different observables during isothermal relaxation runs. The temperature was quenched suddenly from $T = 1.0$ to the value indicated in the caption. There is one exception: The configuration of the highest temperature, $T_c = 0.8$, was annealed after 10 000τ from $T_c = 0.7$. This leads to the formation of a single baby nucleus (see below). Shown are instantaneous values of one configuration sampled every 50τ (except Figure 2e, where an average over 10 configurations is taken).

Figure 2a shows the volume V per monomer. It decreases by about 6−8%. At the two highest temperatures, an induction time is observed, after which structure formation sets in. For the other temperatures, structure formation starts immediately. There is no big difference in the final volume at the different T_c. However, the highest temperatures seem to lead to the smallest final volume. The structure factor discussed in the next section exhibits clear Bragg peaks of (liquid) crystal order. We thus use the terms crystallization and structure formation synonymously in the following. At the end, there is still a small negative slope in $V(t)$. This indicates that the structure formation process is not yet finished. In fact, it will continue to optimize the space filling locally. However, this process eventually becomes very slow. During this so-called secondary crystallization, the global structure of the crystal will be affected only very little. For example, we determined the melting temperature and average stem length at $T_c = 0.74$ and $T_c = 0.70$ already at $t = 80\,000\tau$. Almost no variation

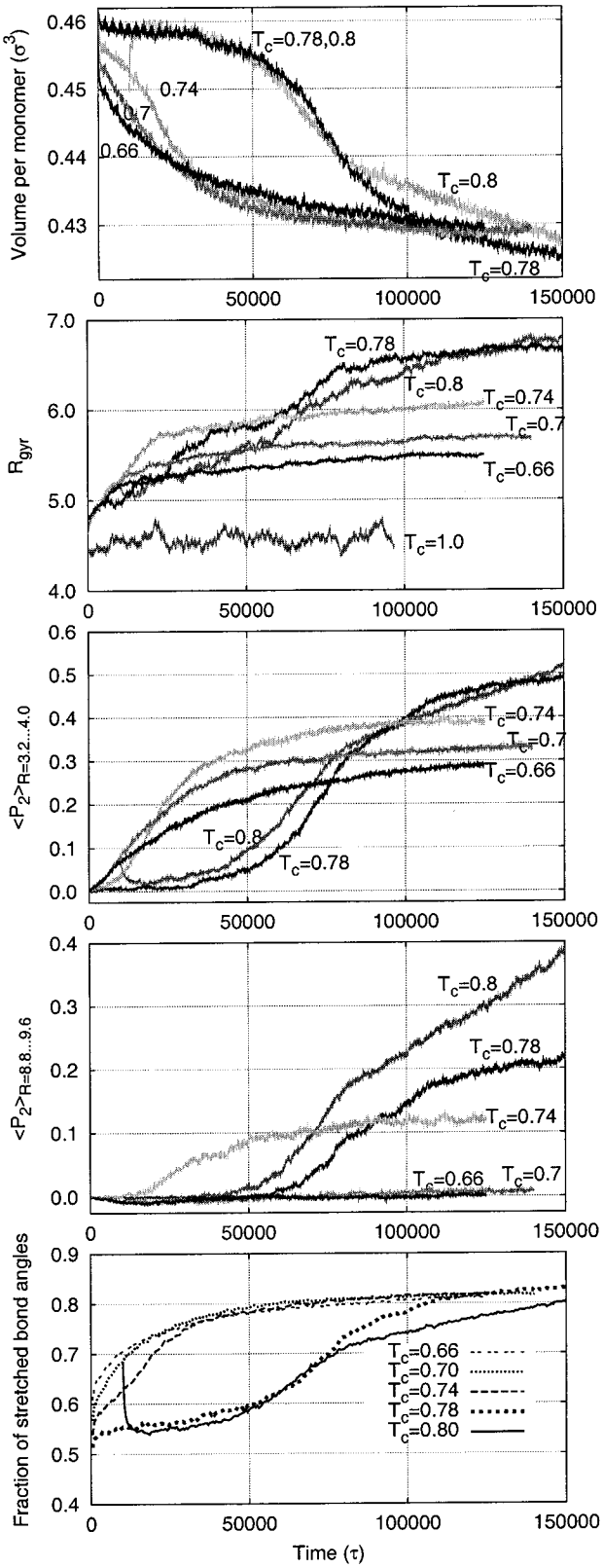

Figure 2. Evolution of observables during isothermal crystallization: (a) volume per monomer, (b) radius of gyration (also shown the value in the melt at $T = 1.0$: R_g fluctuates around 4.6 σ), (c) bond order correlation function in the range 3.2−4.0 (near range order), (d) bond order correlation function in the range 8.8−9.6 (far range order), (e) fraction of stretched bond angles (conformational order).

was seen with respect to the value obtained after the complete simulation time. In addition, in our simulation, the final relaxation will probably be strongly influenced

by the boundary conditions and does not give further insight. We thus decided to stop simulation at the given point since the structural quantities shown in Figure 2 appear sufficiently stable. However, we conclude that our data should mainly be interpreted as the result of the primary crystallization process.

Figure 2b shows the evolution of the mean radius of gyration R_g. Here, a much larger difference with temperature can be observed. In the beginning, R_g increases for all T_c at about the same rate. But the final value is quite different: the larger T_c, the larger the increase of R_g. For comparison, the evolution of R_g in the high-temperature phase is also shown. There are significant fluctuations, but the mean value remains constant. The increase of R_g during crystallization is due to the still rather short chain length. In the crystal, every chain has only a few stems; its global structure is thus considerably changed with respect to the coil state in the melt. For much longer chains, the crystal ordering would affect each chain on a rather local scale, and R_g is expected to remain almost constant.

The next two graphs show the orientation correlation function

$$P_2(R) = \langle 1.5(\vec{U}_i \cdot \vec{U}_j)^2 - 0.5 \rangle_{R=|\vec{R}_i - \vec{R}_j|} \qquad (1)$$

of bond vectors $\vec{U}_i$ and $\vec{U}_j$ averaged in a certain distance region ($\vec{R}_i$, $\vec{R}_j$ are the positions of the two bond vectors $\vec{U}_i$, $\vec{U}_j$). This second Legendre polynomial has some similarities with the order parameter in nematic liquid crystals: $P_2 = 1$ for parallel orientation, $P_2 = -0.5$ for orthogonal orientation, and $P_2 = 0$ if there is no orientation correlation. Figure 2c indicates near range order since the average is made over bond pairs a distance of 3−4 chain diameters apart. The temperature dependence of the near range order resembles that of the volume: the lower the temperature, the faster some order is formed. However, the final order is better the higher the temperature. Figure 2d shows a more distant range order averaged at the distance of about 9 chain diameters (which is almost half the simulation box). In this range, there is no order at all for the lower temperatures. At early times, there is even a slightly negative correlation which indicates that chains or domains tend to be perpendicular to each other at this distance.

Figure 2e shows the fraction of fully stretched bond angles. Its behavior is similar to the volume, but with inverse sign. Note that the total fraction of stretched angles in the final configuration is almost the same at all temperatures. However, as indicated by the differences in R_g and the orientation correlation P_2, the local distribution has to be rather different at different temperatures! From the global fraction, one deduces about $^1/_6$ of not stretched angles. They are localized on the fold surface, thus allowing completely stretched stems of 20 ($T_c = 0.7$) up to 40 monomers ($T_c = 0.8$).

Though the final volume and the total fraction of tt angles are quite similar for all crystallization temperatures, the structures of the crystal formed are quite different (compare e.g. Figures 7a with 9b or Figure 3 of ref 35). This can be understood in the following way: By lowering the temperature, the chains become stiffer and their radius of gyration increases. For the low temperatures, local order is formed very quickly. This fixes the chains locally, and they cannot relax on larger scales. This leads to poor quality of the global crystal.

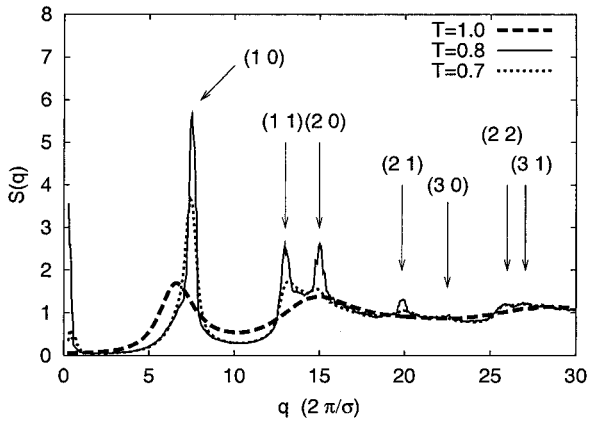

Figure 3. Static structure factor $S(q)$ at $T_c = 1.0$, 0.8, and 0.7. The Bragg peaks of the (2D) hexagonal lattice (indicated by arrows) are more pronounced at smaller supercooling.

At higher temperature, crystallization only starts after some induction time. During this induction time, the radius of gyration already increases; a first nucleus has to fight more against the thermal motion (lower nucleation probability). However, when it has reached its critical size and starts to grow, better crystals are formed than at lower temperature.

3.2. Evolution of the Structure Factor. A quantity that permits a direct link to experiments is the static structure factor

$$S(q) = \left\langle \frac{1}{m} \sum_{j=1}^{m} \exp(i\vec{R}_j \vec{q}) \right\rangle_{|\vec{q}|=q\pm dq} \qquad (2)$$

The sum goes over all m monomers in the system, and the average is taken over all vectors $\vec{q}$ of length $q \pm dq$. The figures shown below are usually calculated with bin size $dq = 0.01\sigma^{-1}$; a running average is applied in the interval $q_r = \pi/L$ where L is the box size. In addition, the average over four frames is taken. To avoid artifacts in the structure factor, only scattering vectors that are compatible with the periodic boundary conditions may be used. This implies that only vectors on a cubic lattice with spacing $q_L = 2\pi/L$ are available. At low q, only few vectors enter the average, and the precision is not as good as for larger scattering vectors ($q > 1$). However, the peak in $S(q)$ observed at $q < 1$ is well compatible with the average thickness of the lamellar-like structures calculated below by the intrachain bond-correlation function.

Figure 3 compares $S(q)$ of the final structure obtained at $T_c = 0.8$ and $T_c = 0.7$ with the melt at $T = 1.0$. The high-temperature curve shows the typical liquid structure whereas the low-temperature curves exhibit Bragg peaks in the ratio $1:\sqrt{3}:2$ characteristic of the hexagonal lattice. These peaks are more pronounced at higher T_c where even higher orders can be identified. In our model chains have a more or less cylindrical structure. Thus, they should arrange in a hexagonal lattice (see the cut through snapshots of Figure 10). At lower temperature, the crystal domains are smaller and so is the range of the order. This is the reason for less pronounced peaks at $T_c = 0.70$.

Figure 4 shows the evolution of $S(q)$ for $T_c = 0.78$ obtained from a simulation box with 1000 chains, thus 5 times larger than used for the data in the preceding sections. The side length of the box corresponds to $q =$

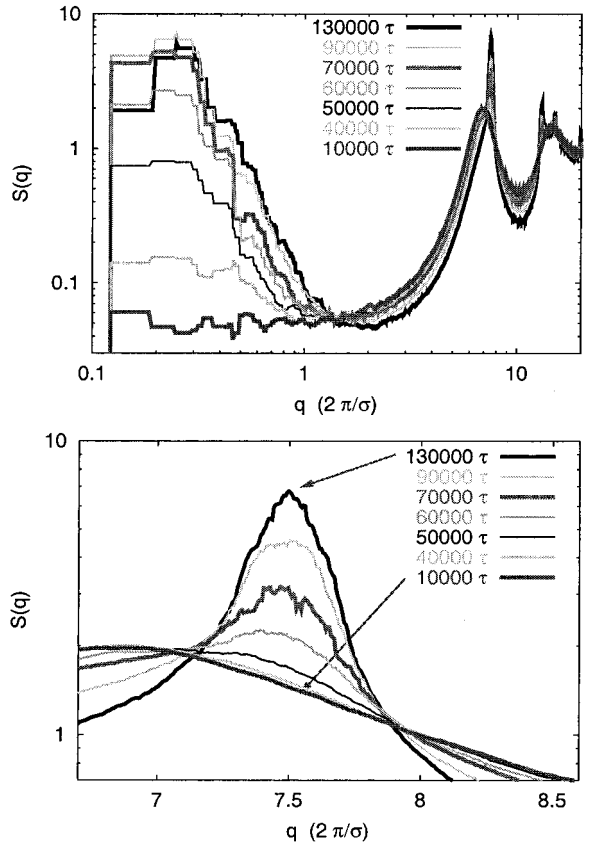

Figure 4. Evolution of $S(q)$ at $T_c = 0.78$. (a) Double-logarithmic representation to highlight the region for small q. (b) Detail of the first main peak growing at $q = 7.5$. Up to $t = 30\,000\tau$, there is no change. Then the peak at $q < 1$ grows rapidly whereas the peak at $q = 7.5$ is less pronounced in the beginning.

0.17. Until $t = 30\,000\tau$ there is no evolution; $S(q)$ exhibits the liquid structure. During the next $10\,000\tau$, a first nucleus forms which takes 0.2% of the total volume (according to the definition of local order used in section 3.4). At $t = 40\,000\tau$, the intensity of $S(q)$ has doubled at $q < 1$ whereas at $q = 7.5$, one observes only an increase by the thickness of the line. At $t = 50\,000\tau$, the volume fraction of crystal points is about 1%, and the appearance of a peak at $q = 7.5$ is clearly seen. This behavior is consistent with experimental observations that SAXS is more sensitive than WAXS. References 13 and 14 for example conclude that their WAXS experiments have a lower detection limit of about 0.5−1% crystallinity.

To better quantify the evolution of the scattering intensities, we calculated the integral of $S(q)$ in certain q regions. Figure 5 shows this integrated intensity below the small-angle scattering peak ($q = 0.3-0.9$) and below the second-order Bragg peak at $q = 13$. The figure shows data for the small box with 19 200 monomers as well as data for the big box with 100 000 monomers (at $T_c = 0.70$, the big system was only simulated for $50\,000\tau$). The data of both box sizes superpose quite well, indicating that already the small box may permit a reasonable estimate for the onset of structure formation. One sees again that, at the lower T_c, structure emerges immediately whereas at $T_c = 0.78$ nothing happens up to $t = 35\,000\tau$.

At the beginning, the small-angle intensity increases quite fast contrary to the wide-angle intensity. The slope

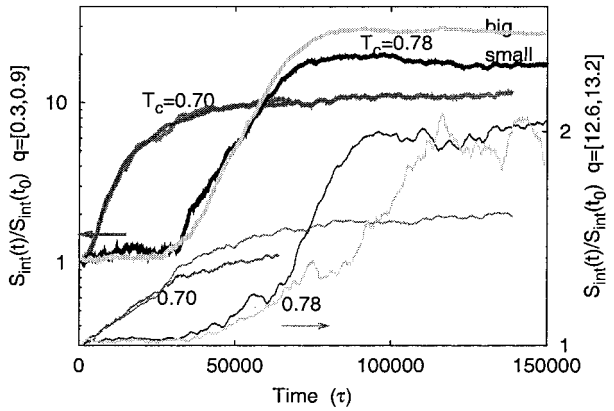

Figure 5. Evolution of the intensity of the low-angle scattering peak (thick lines: $S(q)$ integrated for $q = 0.3-0.9$) and a second-order Bragg peak (thin lines: $S(q)$ integrated for $q = 12.6-13.2$). Shown are data for two temperatures $T_c = 0.70$ and $T_c = 0.78$ and for each temperature the data of two different simulation box sizes. The data of these different box sizes superpose quite well.

of the wide-angle intensity increases only considerably when the small-angle intensity reaches already its maximum value. This behavior is particularly pronounced at $T_c = 0.78$. We interpret this behavior in the following way: The formation of a baby nucleus represents a large-scale density fluctuation while it contains only little crystalline order. Thus, the wide-angle scattering intensity can only increase considerably when the nucleus grows laterally (more stems being attached). However, at that moment, its large-scale shape does not change much further. In summary, we do not observe a significant delay between the onset of increase in small- and wide-angle scattering intensity. However, the wide-angle scattering intensity initially grows very slowly and could indicate an underlying two-step process.

3.3. Cooling and Heating at Constant Rate. The second "experiment" concerns relaxation during cooling at constant rate. In Figure 6 the same quantities as for the isothermal relaxation runs are reported, now as a function of temperature. Three different cooling rates are used convering 1 decade (see Table 1). The graphs also contain the data of melting of the final configurations obtained by isothermal relaxation. The melting runs are all performed with the fast heating rate $2 \times 10^{-5}\tau^{-1}$. Several observations can be made:

(i) Comparing cooling and heating curves, one sees a large hysteresis in all quantities. This is a common phenomenon of first-order phase transformations. According to classical nucleation theory, there is a competition between the gain of bulk free energy of the new phase and the energy cost of forming an interface between the old (melt) and the new (crystal) phase. One needs to overcome an energy barrier to form a "critical" nucleus of the new phase which is stable and large enough to continue growing. The larger the supercooling, the lower the barrier and the larger the nucleation density. The difference between crystallization and melting temperature is thus enforced by the fast cooling rates and the small box size. With the cooling rates employed one passes rapidly over the temperature regime where one would have to wait too long for one nucleation event to take place. Once a crystal fills the whole simulation box, it is stabilized by the periodic boundary conditions. This increases the observed melting temperature. By contrast, lower heating rates can lead to annealing of the crystal. For the determination

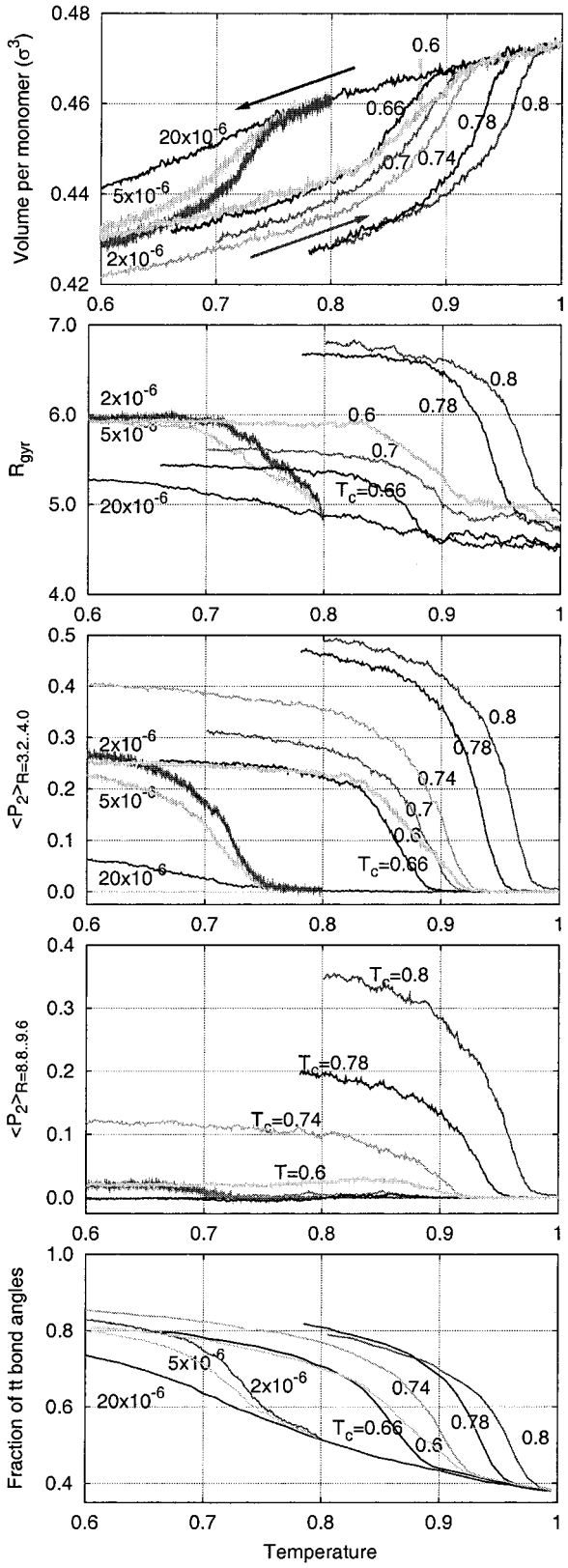

Figure 6. Cooling at constant rate and melting of configurations obtained after isothermal relaxation: (a) volume per monomer, (b) radius of gyration, (c) bond orientation correlation function in the range 3.2−4.0 (near range order), (d) bond orientation correlation function in the range 8.8−9.6 (far range order), (e) fraction of stretched bond angles (conformational order).

of T_m of the structures obtained at isothermal relaxation, we chose a heating rate at which no annealing effects were observed. Otherwise, the T_m would correspond to a different structure.

(ii) Let us consider now the cooling curves. Cooling at $2 \times 10^{-5}\tau^{-1}$ is too fast for crystallization to set in. Only a very poor near-range order is observed. We estimate the glass transition temperature for this model to be below $T = 0.5$. Already around $T = 0.6$ dynamics is very slow, and almost no increase of the order is observed. Figure 2a suggests that the major change of the phase transformation lasts around 40 000τ. The rest of the time, the system performs local optimization (or "preparation" during the induction time at higher T_c). At the fast rate, where the range from $T = 1.0$ to 0.5 is scanned in only 25 000τ, there is not enough time for structure formation. At the intermediate and the slow rate, thus a factor 4 or 10 slower, the time spent at higher temperatures is sufficient for structure formation to set in. It starts in both cases at $T = 0.75$ whereas in isothermal runs, also at $T = 0.78$, homogeneous nucleation was observed after reasonable waiting time. The runs at the slower cooling rates have been started from $T = 0.8$ from an intermediate configuration obtained from cooling at the fastest rate. We started also one run at the intermediate cooling rate from $T = 1.0$: Nothing changed in the high-temperature region, and the order formation also sets in around $T = 0.75$. The same observation was made for a system 5 times larger. This suggests that at the given cooling rates neither the small box size nor the thermal history above $T = 0.8$ has much influence on the nucleation process. It is the temperature-dependent chain dynamics which controls the structure formation.

(iii) The melting curves are nicely ordered according to the temperature at which the configuration was obtained: The lower T_c, the smaller the average stem lengths (completely stretched segments) and the lower the melting temperature. The T_m of Table 1 is obtained by the location where a linear extrapolation of the largest slope of $V(T)$ cuts the volume of the amorphous state. This is an upper limit of T_m.

(iv) There is one exception: the light gray curve which is the melting curve of the configuration obtained after cooling at the intermediate rate down to $T = 0.6$. (At $T = 0.6$, we waited for 40 000τ; however, the increase in order is negligible.) This melting curve has a different slope when reaching the value of the amorphous phase. Visual inspection of the configuration shows that one initial nucleus with very long stems was formed at the beginning. As the temperature decreases further, the rest of the chains crystallize with very short stems. The crystal formed in this way is thus inhomogeneous, and the melting takes place over a larger temperature range. During the melting, the short stems melt first. One can even observe an annealing effect: the long-range order increases slightly above $T = 0.8$, just before the long domain melts also.

(v) The configuration crystallized at $T_c = 0.74$ was also further cooled at the same rate as the melting curves. There is still a small increase in local order and in the fraction of stretched bond angles. On a larger scale as seen by the radius of gyration and the long-range order parameter, there is almost no further structural change.

After these average results for the melting process, Figure 7 shows a sequence of snapshots. They are obtained from continuous heating of the configuration obtained by isothermal relaxation at $T_c = 0.70$. In the first snapshot, a large domain perpendicular to the cut

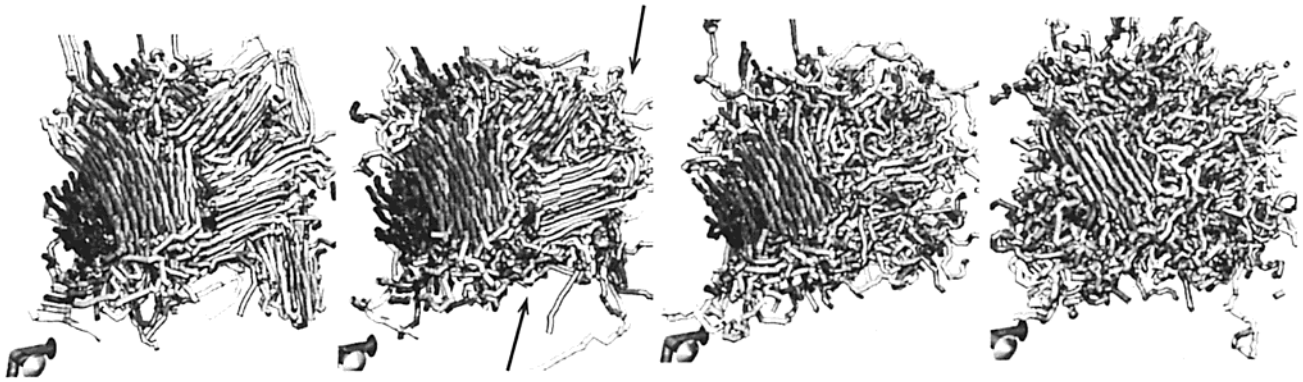

Figure 7. Snapshots during the melting of a configuration obtained by isothermal relaxation at $T_c = 0.70$ with 192 100-mers. Heating is performed at rate $10^{-5}\ \tau^{-1}$; the figures correspond to $T = 0.81$, 0.85, 0.87, and 0.89 (from left to right). Shown is a cut through the configuration; note that periodic boundary conditions apply in the remaining directions. The chains on the interface between domains start to melt first as indicated by arrows. The large domain on the left of the configuration resists longest.

plane can be seen on the left and two further domains on the right which are almost parallel to the cut. Up to about $T = 0.85$, nothing changes. Then, one can observe several chains becoming disordered (arrows in the second snapshot): The melting starts at the interfaces between the crystal domains. The smaller domains melt rapidly, whereas one can follow the shrinking of the large domain on the left of the configuration. As one may expect, the melting proceeds from the outside to the interior of the domain.

3.4. Analysis of Crystallized Domains. We come now back to the process of structure formation and analyze the formation of domains of different orientation. This requests an algorithm based on a local order parameter to determine the ordered domains: For a given point R, calculate first the average orientation of all bond vectors in a small box of side length b. The local order parameter is then determined as the average of the second Legendre polynomial of the cosine between this average orientation and all bond vectors in a box of side length a. Both boxes have the same center R but may have different size. A point R is called ordered, if the order parameter is larger than a certain threshold value d. In the following, we use $b = 3.4$ chain diameters and $a = 4.7$ chain diameters. A threshold value is chosen $d = 0.85$, which corresponds to an average deviation of less than 20°.

The local order parameter is now calculated on a cubic lattice of 30^3 points. On this lattice, we determine percolating clusters of ordered points. Each cluster is identified with one domain. (We do not check the orientation of neighboring "ordered" points. Visual inspection showed that the chosen parameters yield a very strong definition of order and that the interface between domains is always classified as disordered.) Clusters with less than 25 points are discarded; they correspond to domain sizes of less than 2 chain diameters which result from local fluctuations. Only a few large domains remain stable and grow with time. The evolution of the volume fraction involved in ordered clusters obtained by this analysis is shown in Figure 8. For each crystallization temperature the total volume fraction occupied by all ordered points is plotted. Big symbols mark the evolution of the largest domain. The total ordered volume fraction is largest for the highest T_c. This trend resembles that seen in Figure 2. In the representation of Figure 8, however, the variation with T_c is much more pronounced. This is due to our definition of crystallized domains where the interfaces between ordered domains take quite a large volume fraction. The relative size is also interesting if several clusters are found in the same system. At $T_c = 0.78$, only one domain starts to grow. After some time, a second domain develops, and the plus signs of the largest cluster do not coincide with the line of the total volume fraction any more. At the lower temperatures, several domains start to grow almost from the beginning. Consequently, they are much smaller. In the final configuration, three domains can be distinguished at $T_c = 0.74$ and $T_c = 0.70$ and four domains at $T_c = 0.66$.

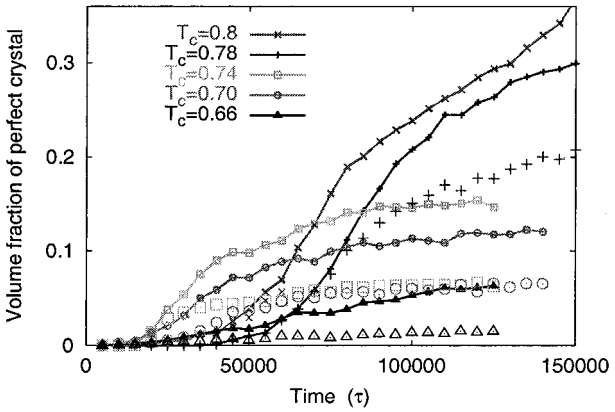

Figure 8. Evolution of the volume fraction of crystallized domains (lines with small symbols). Big symbols represent the largest domain of the corresponding T_c.

At $T_c = 0.8$, we observe only one domain which finally percolates through the whole simulation box. In fact, the change in slope at about 80 000τ, which can also be observed in Figure 2, coincides with the time when the crystal domain grows laterally into its periodic image and fills the whole simulation cell. In this case, the pressure tensor becomes anisotropic. As a consequence, the stems take on a larger angle with respect to the axes of the simulation box. At $T_c = 0.80$ we repeated the calculation from the moment when the crystal domain percolates through the simulation box, but now with independent pressure coupling in the three dimensions. In this case, the shape of the box changes considerably. It extends almost 10% in the direction of the stems and shrinks laterally by about 10% because the stems tend to align parallel with the simulation box. The average stem length increases only slightly. At the other temperatures, where several domains develop, the change in the quantities of Figure 2 is more gradual, and the pressure tensor always remains isotropic.

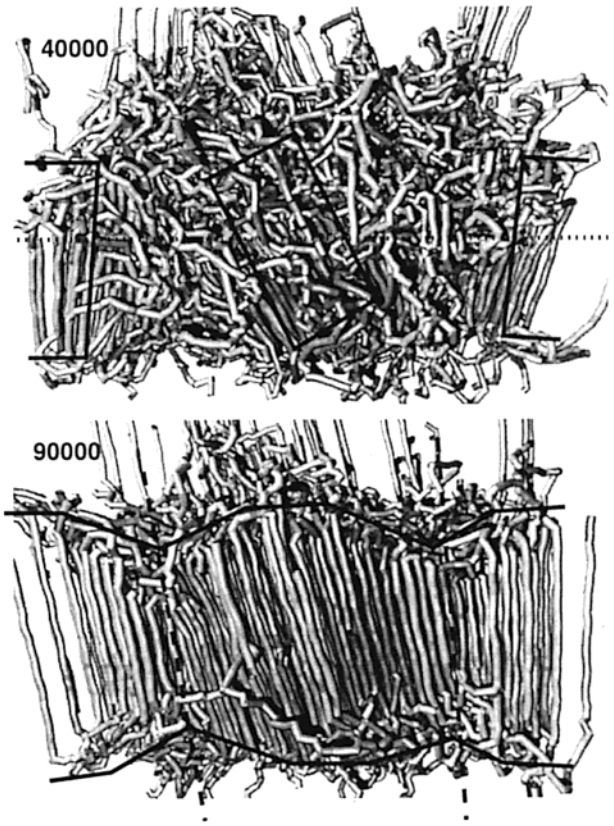

Figure 9. Doubled box (384 100-mers) during isothermal relaxation at $T_c = 0.8$. Note that periodic boundary conditions apply. The chains are not cut but mapped with their center of mass into the central box. Top: $t = t_0 + 40\,000\tau$, bottom: $t = t_0 + 90\,000\tau$. At the beginning, the two nuclei grow independently; their orientation is indicated by the black rectangles. When they start growing into each other, the chain orientation aligns with each other. However, one can recognize that the thickness is still smaller at the interface between the two blocks.

3.5. Merging of Blocks. To check for finite size effects and to study the merging of crystal domains, one larger box was simulated. Since we got a well-defined nucleus at $T_c = 0.8$, we take the same configuration at $t_0 = 20\,000\tau$ and duplicate it laterally. The simulation box is now rectangular, and we use independent pressure coupling in the three dimensions. At the very beginning, the two halves of the simulation box are identical, but soon their evolution differs because the random noise of the thermostat uses different random number sequences in the different regions. The result is that the two baby nuclei develop in different orientations as indicated in Figure 9. When the domains touch each other, the stems start reorienting, and the two domains finally align parallel to each other. However, the interface between the two initial domains remains visible for quite a long time. The bottom part of Figure 9 is a snapshot taken at an intermediate time when the domains are already fairly parallel. (There is an additional distortion due to the projection—the chains on the very left and the very right are neighbors because of the periodic boundary conditions and strictly parallel.) The average thickness profile is indicated. When we stopped the simulation after $t_0 + 130\,000\tau$, many stems are still shorter in the interfacial region. Figure 10 shows a cut through the simulation box. In this plane, the two nuclei are visible from the beginning, and one can follow their growth. Figure 9 shows the top side of these cuts.

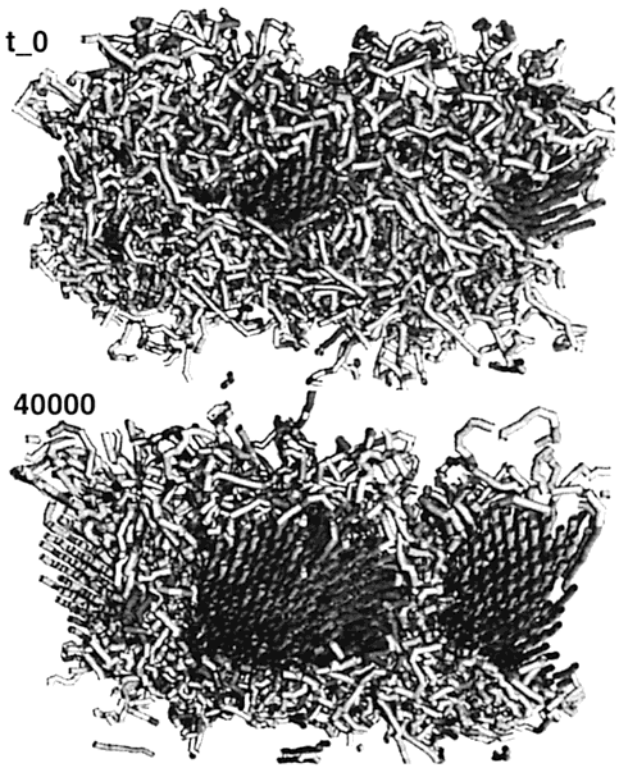

Figure 10. Cut through the double box of the isothermal relaxation at $T_c = 0.8$. Top: the initial nuclei at $t - t_0 = 0$. Bottom: an intermediate configuration at $t_0 + 40\,000\tau$ (Figure 9a contains the corresponding side view). The two nuclei are growing into each other.

3.6. Distribution of Conformational Order along the Chains. Figures 2e and 6e show the total fraction of stretched bond angles. In fact, this does not tell anything about their distribution along each chain. According to these statistics, one should have on average sequences of six stretched angles. Visual inspection of crystallized configurations reveals that most chains are folded with quite long stretched stems. Histograms of the number of successive stretched angles allow a more quantitative analysis. While there are almost no stems longer than 10 monomers in the amorphous melt, more than half of the monomers are involved in stems longer than 20 monomers at the end of the crystallization at $T_c = 0.78$ and still longer than 12 monomers for crystallization at $T_c = 0.66$.

Next we analyze the loops and folds. For this, we have to specify an algorithm how to detect them: We define a "fold" to be the region between two stems A and B of at least eight successively stretched bond angles on the same chain. One fold may thus contain several non-tt angles as well as short tt sequences. The distance between two successive stems A and B is defined as the number of angles between these stretched stems. The relative orientation is determined by the cosine between the last bond vector of stem A and the first bond vector of stem B. According to the value of this cosine, we define five fold classes:

$$-1.0 \le \cos(AB) < -0.8 \quad \text{back fold} \tag{3}$$

$$-0.8 \le \cos(AB) < -0.5 \quad \text{almost back fold} \tag{4}$$

$$-0.5 \le \cos(AB) < 0.5 \quad \text{orthogonal fold} \tag{5}$$

$$0.5 \le \cos(AB) < 0.8 \quad \text{almost step fold} \tag{6}$$

$$0.8 \le \cos(AB) \le 1.0 \quad \text{step fold} \tag{7}$$

Our algorithm might miss some folds; however, visual control of several chains suggests that it is quite reliable. The statistics does not change significantly if one varies the minimum length of successive stems for the definition of a fold between 6 and 10. Figure 11 shows the evolution of the number of folds according to this classification for the isothermal crystallization run at $T_c = 0.78$. One sees the number of folds increasing to almost two folds per chain (on average). Most of them are back folds. There is still a considerable number of orthogonal folds (almost one for every second chain). The remaining folds are equally distributed among the remaining three classes. Further discrimination among the back folds reveals that most of them are tight folds; i.e., the chain reenters the same crystal domain in the near neighborhood. A large number are actually hairpin folds where the two successive stems are nearest neighbors. Less than 30% of the back folding stems reenter the crystal at distances further away than three chain diameters.

Figure 12 compares the final distribution of folds at several temperatures. The trend is clear: the lower the temperature, the more folds are present. At lower temperatures, the number of folds per chain increases to about 2.5. The relative distribution of folds remains the same, however, with a tendency to tighter folds. One qualitative difference can be observed for the orthogonal folds which are due to chains having stems in domains of different orientation. At lower temperatures, there are several domains, whereas at $T_c = 0.8$, there is only one; thus, the number of orthogonal folds is very small. Figure 13 shows typical single chain conformations to illustrate the different types of folds. The chain ends are mostly located near the surface of the ordered domains.

Because of the small box size, the ordered domains are approximately as large as thick, and one may question to call them "lamella". However, it is possible to define an average stem length via the intrachain bond orientation correlation function

$$P_1(k) = \langle \vec{U}_i \cdot \vec{U}_j \rangle_{|i-j|=k} \tag{8}$$

where $\vec{U}_{i,j}$ are two bond vectors on the same chain but k monomers apart. The average is taken over all pairs of bond vectors of the same chain with distance k and over all chains. In the melt, this correlation function decays exponentially. It is usually used to determine the persistence length. Figure 14 shows this correlation function for the isothermal crystallization runs. In the crystal phase, the exponential shape is lost, and $P_1(k)$ exhibits oscillations according to the (average) number of folds per chain. The first minimum gives an estimate of the average stem length; this means the fully stretched parts of a chain. The value obtained in this way is reported in Table 1. We use this average stem length as an estimate of the lamellar thickness. The fact that there is a majority of back folds makes the minimum of P_1 well-defined. This minimum may overestimate the stem length slightly because it includes the bonds involved in the fold. However, since most back folds are rather tight, this error is small.

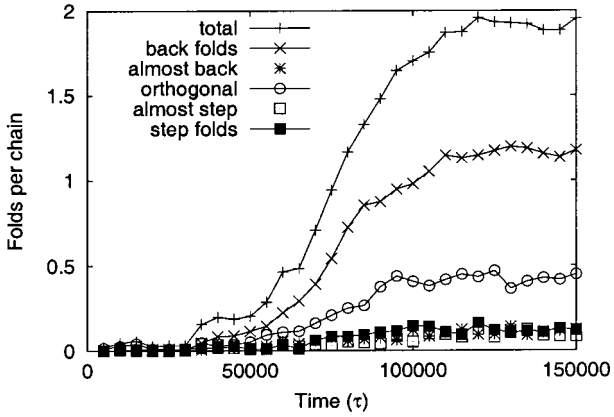

Figure 11. Evolution of the number of folds per chain for isothermal relaxation of 100-mers at $T_c = 0.78$. Most folds between stems (sequences of at least eight tt angles) are back folds; i.e., the chain reenters the same crystal domain. The next group are orthogonal folds linking stems in different domains orthogonal to each other. The other kinds of folds are less frequent, indicating that the crystal order is rather good.

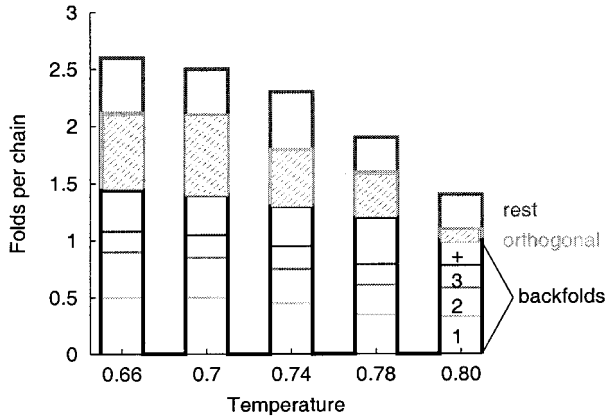

Figure 12. Types of folds in the final structures at different crystallization temperatures. The back folds marked 1 are hairpin back folds, 2 means that the stem reenters as a second neighbor, etc. (see text).

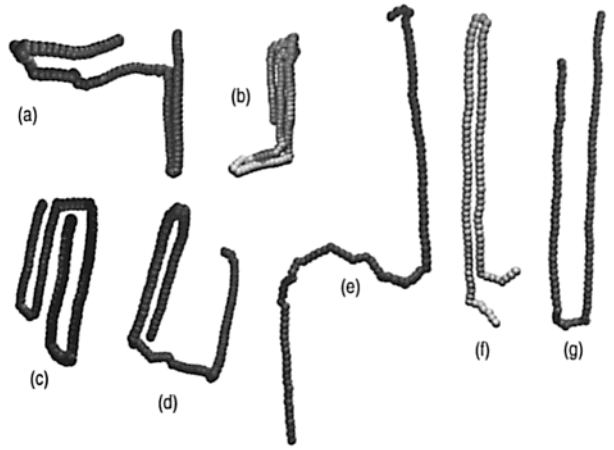

Figure 13. Typical single chain conformations in the final configuration at $T_c = 0.70$ (a–d) and $T_c = 0.80$ (e–g). (a) and (b) have orthogonal and hairpin folds, (c) has three back folds, (d) two back folds and a larger bridge, (e) has a step fold with a large bridge in the fold surface, (f) a hairpin fold, and (g) a back fold reentering at the third neighbor.

4. Discussion

4.1. Crystallization and Melting Line. Figure 15 presents the data collected in Table 1. At a given

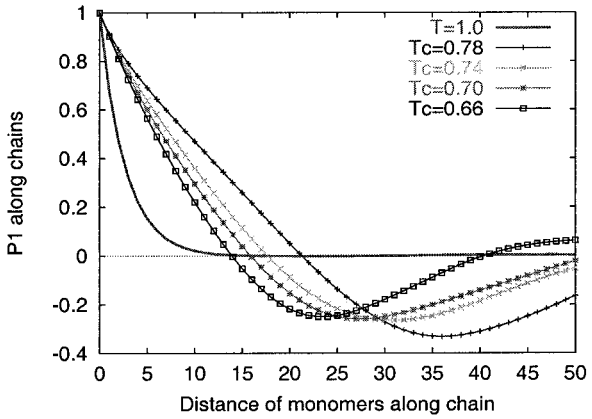

Figure 14. Intrachain orientation correlation function $P_1(k)$ at the end of isothermal crystallization of the 100-mers. In the melt at $T = 1.0$, this function is approximately exponential, yielding a persistence length of 3.5 monomers. In the crystal, the first minimum gives an estimate of the average stem length.

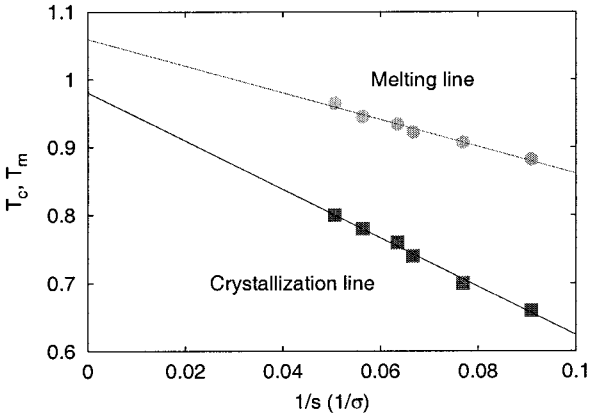

Figure 15. Crystallization (squares) and melting (circles) temperatures vs inverse stem length s. The lines are linear fits. One observes well-defined crystallization and melting lines.

temperature T_c, the system relaxed isothermally, and a structure of average thickness s was formed; the points $T_c(1/s)$ form the crystallization line in Figure 15. The subsequent melting was performed at a sufficiently high rate such that no annealing occurred (data in Figure 6a). These melting temperatures are rather overestimated; however, they have been obtained consistently in the same manner for all systems.

Interestingly, both T_c and T_m are proportional to the inverse stem length $1/s$, however, with a different slope. The kind of representation given in Figure 15 is used in the discussion of the crystallization process by Keller[4,19] and Strobl.[6] The melting line is attributed to the Gibbs−Thomson relation supposing the structure of length s in thermodynamic equilibrium with the melt. The crystallization line is probably rather of kinetic origin; however, its explanation is still under debate.[41] The extrapolation $1/s \rightarrow 0$ of the two lines does neither meet nor cross as in most experimental works.[4,6] This is probably due to finite size effects but could also be a feature of the short chain length.

It may surprise that we find a well-defined crystallization line at all. Our chains of $N = 100$ monomers can be compared with $C_{201}H_{403}$. For n-alkanes of this length, one would expect integer chain folding, i.e., the length of an extended chain should be an integer multiple of the lamellar thickness; this would yield steps

Figure 16. Snapshots of six chains during the evolution of a baby nucleus: The chain in the center (arrow) is collapsed and forms a critical nucleus (left). It rapidly grows in length; at the same time, further chains start to align laterally (center). At the right, the same chains are shown in the final crystal.

rather than a straight line for $T_c(1/s)$. (Integer chain folding was also shown in ref 34 to appear in UA model chains in solution.) We also recognize a tendency to integer chain folding. In fact, we expect that for much longer simulation times, the obtained structures would converge further toward lamellae whose thickness would correspond to an integer number of folds with the chain ends well aligned at the fold surface. If one simulated at intermediate temperatures, one should finally obtain steps in the $T_c(1/s)$ diagram, at least for the higher temperatures. Since we suppose our data to represent the crystal state at the end of the primary crystallization, the given crystallization line is probably still a good approximation. However, a continuous crystallization line is certainly expected for longer chains when the number of folds is large such that the influence of chain ends becomes negligible.

4.2. Nucleation. Visual inspection of snapshot sequences leads us to the following picture of the starting point of a crystal domain. When lowering T, due to the angle bending potential (Figure 1), the stretched tt state becomes more populated. At low T, the barrier between the tt and gt state becomes harder to overcome, and the chains stiffen. (The persistence length of a free chain at $T = 1.0$ is 3.4 monomers vs 6 monomers at $T = 0.7$.) Coming from the melt, the chains have to stretch locally, which leads to localization of kinks and the formation of folds because relaxation to completely stretched chains would require a disentanglement and thus much longer times. Mostly, we identified intrachain nuclei as the very starting point of crystal growth. If there is a compact part of a chain with one or two folds, it may rapidly grow in length and then induce chains in the neighborhood to align with this ordered (micro)domain (see Figure 16). The critical nucleus found by visual inspection has usually a stem length of about 15−20 monomers and at least 2−4 stems, thus approximately 50−80 monomers. The weaker the supercooling, the less the chains are perturbed with respect to their equilibrium conformation and the less pronounced is the local stretching which may lead to a small baby nucleus. At $T_c = 0.78$, the induction time is long. At this temperature, simulations with two different box sizes (192 chains and 1000 chains) checked the influence of the finite size. In both cases, the first nucleus formed at about the same. This is an indication that no significant artifact is introduced for the early structure formation by the small box size and that the nucleation is determined by the relaxation of the chains.

The simulation at $T_c = 0.8$ used a sort of "self-seeding" technique: the system was first quenched to $T = 0.7$. After waiting for 10 000τ, temperature was raised to 0.8.

During the short time at $T = 0.7$, several baby nuclei are formed which melt immediately after raising the temperature. However, one nucleus remains and starts growing as visualized in Figure 5 of ref 35. The domain emerging from this nucleus eventually fills the whole simulation box (Figure 3b in ref 35). The same nucleus was used for the experiment of block merging in section 3.5.

For further comparison with experimental data, it would be interesting to study still weaker supercooling. However, the expected structures will be even larger and one must use larger simulation cells. Probably, it is then also necessary to introduce (predefined) heterogeneous nuclei, since otherwise the induction time would be too long.

4.3. Finite Size Effects. The finite size of the system should play a role. A chain certainly interacts with its periodic image if the size of the crystallites is of the order of the simulation box. In addition, the length of a fully stretched chain is about twice the side length of the smaller simulation box used to obtain Figure 15. However, we think that this effect is rather small and probably negligible below $T_c = 0.78$. At least the early stage of structure formation and the crystallization line are probably not influenced by finite size artifacts because the crystallites grow in arbitrary directions with respect to the box coordinates. However, we expect that the formation of domains orthogonal to each other and especially the formation of smaller domains at the end of the primary crystallization process is enhanced by the small system size. The box is rapidly filled by the larger domains with no space left between their periodic images. Thus, with the present simulation boxes, the intermediate phase of crystal growth where a crystal front (which is not necessarily sharp) is in coexistence with the melt can hardly be isolated. The simulation is dominated by the nucleation event and then by the secondary crystallization where space filling is optimized. Finite size effects should also influence the melting temperatures. Especially when one single domain fills the simulation box as for $T_c = 0.8$, the periodic boundary conditions stabilize the structure since the domain has no lateral surfaces where the melting can start.

5. Conclusions

The MD simulation data described in this paper show that the model CG-PVA exhibits a reasonable temperature dependence of the structure formation in supercooled melts. Though the interaction potentials of the model were initially fitted to describe PVA, the used model is a rather generic one at the level of approximations discussed in section 2.2. However, this simple model contains enough physics to lead to very interesting crystallization-like behavior. Because of the absence of explicit attractive interactions, the ordering transition is mainly entropically driven by a liquid-crystalline-like packing transition. However, there is still an energetic component through the angle bending potential.[35]

We conclude with some speculations on what can be deduced from this study concerning the ongoing discussion about the polymer crystallization process, namely the spinodal-assisted crystallization[10] or Strobl's block picture?[6] For the model and the systems examined here, we observe rather classical nucleation and growth of the crystal domains. The discussion of the static structure factor showed no significant delay between the onset of large-scale (lamellar) structure and local crystal structure. However, initially the small-angle scattering intensity grows much faster than the wide-angle Bragg peaks. In this sense, our data rather support the interpretation of ref 14 that the delay between small- and wide-angle scattering signals may be due to experimental difficulties of resolving very low crystallinity.

Concerning the "block picture" proposed by Strobl,[6] Figure 9 may support a possibly granular structure of lamellae. However, one should be careful because the figure was obtained by introducing two nuclei which then grew into each other. This is different from the scenario supposed by Strobl where new blocks should emerge out of a mesomorphic layer in front of the already existing granular lamella.

For further advances, the present study must be extended in two directions: larger simulation boxes and longer chains. We simulated a box of about 11−18 nm side length. This corresponds roughly to one block in Strobl's picture. To investigate his hypothesis of block merging from a mesomorphic layer, one should have a simulation box large enough to contain several blocks surrounded by amorphous material. Second, Strobl claims his picture being valid mainly for highly entangled chains. To approach this case, much longer chains have to be simulated. For the present model, we estimate the entanglement length in the range of 50 monomers. The chains of $N = 100$ monomers show clearly the onset of entanglement effects in the mean-square displacement of central monomers. However, entanglements are still weak for this chain length and mostly disappear during the ordering in the crystal structure, at least at the higher T_c where only one or two folds occur per chain. In this case, the crystal lamella affects the global order of one chain. For longer chains, disentanglement would be largely prohibited, and the crystal ordering would take place on a local scale compared with the dimension of one chain. We imagine that this could change some details in the crystallization process with respect to the systems examined here.

Acknowledgment. We thank J. Baschnagel, K. Kremer, B. Lotz, and J.-U. Sommer for fruitful discussions.

References and Notes

(1) Keller, A. *Philos. Mag.* **1957**, *2*, 1171.
(2) Fischer, E. W. *Z. Naturforsch. A* **1957**, *12*, 753.
(3) Keller, A. *Polymer* **2000**, *41*, 8751.
(4) Keller, A.; Cheng, S. Z. D. *Polymer* **1998**, *39*, 4461.
(5) Armistead, K. A.; Goldbeck-Wood, G. *Adv. Polym. Sci.* **1992**, *100*, 221.
(6) Strobl, G. *Eur. Phys. J. E* **2000**, *3*, 165.
(7) Lotz, B. *Eur. Phys. J. E* **2000**, *3*, 185.
(8) Cheng, S. Z. D.; Li, C. Y.; Zhu, L. *Eur. Phys. J. E* **2000**, *3*, 195.
(9) Muthukumar, M. *Eur. Phys. J. E* **2000**, *3*, 199.
(10) Olmsted, P. D.; Poon, W. C. K.; McLeish, T. C. B.; Terrill, N. J.; Ryan, A. J. *Phys. Rev. Lett.* **1998**, *81*, 373.
(11) Ryan, A. J.; Fairclough, J. P. A.; Terrill, N. J.; Olmsted, P. D.; Poon, W. C. K. *Faraday Discuss.* **1999**, *112*, 13.
(12) Akpalu, Y.; Kielhorn, L.; Hsiao, B. S.; Stein, R. S.; Russell, T. P.; van Egmond, J.; Muthukumar, M. *Macromolecules* **1999**, *32*, 765.
(13) Wang, Z.-G.; Hsiao, B. S.; Sirota, E. B.; Agarwal, P.; Srinivas, S. *Macromolecules* **2000**, *33*, 978.
(14) Wang, Z.-G.; Hsiao, B. S.; Sirota, E. B.; Srinivas, S. *Polymer* **2000**, *41*, 8825.
(15) Fu, Q.; Heck, B.; Strobl, G.; Thomann, Y. *Macromolecules* **2001**, *34*, 2502.
(16) Imai, M.; Kaji, K.; Kanaya, T. *Phys. Rev. Lett.* **1993**, *71*, 4162.

(17) Ezquerra, T. A.; López-Cabarcos, E.; Hsiao, B. S.; Baltà-Calleja, F. J. *Phys. Rev. E* **1996**, *54*, 989.
(18) Matsuba, G.; Kanaya, T.; Saito, M.; Kaji, K.; Nishida, K. *Phys. Rev. E* **2000**, *62*, R1497.
(19) Keller, A.; Goldbeck-Wood, G.; Hikosaka, M. *Faraday Discuss.* **1993**, *95*, 109.
(20) Li, L.; Chan, C.-M.; Yeung, K. L.; Li, J.-X.; Ng, K.-M.; Lei, Y. *Macromolecules* **2001**, *34*, 316.
(21) Hobbs, J. K.; Miles, M. J. *Macromolecules* **2001**, *34*, 353.
(22) Sadler, D. M.; Gilmer, G. H. *Phys. Rev. Lett.* **1986**, *56*, 2708.
(23) Doye, J. P. K.; Frenkel, D. *Phys. Rev. Lett.* **1998**, *81*, 2160. Doye, J. P. K.; Frenkel, D. *J. Chem. Phys.* **1998**, *109*, 10033.
(24) Anderson, K. L.; Goldbeck-Wood, G. *Polymer* **2000**, *41*, 8849.
(25) Doye, J. P. K. *Polymer* **2000**, *41*, 8857.
(26) Yamamoto, T. *J. Chem. Phys.* **1997**, *107*, 2653.
(27) Takeuchi, H. *J. Chem. Phys.* **1998**, *109*, 5614.
(28) Fujiwara, S.; Sato, T. *Phys. Rev. Lett.* **1998**, *80*, 991. Fujiwara, S.; Sato, T. *J. Chem. Phys.* **1999**, *110*, 9757.
(29) Shimizu, T.; Yamamoto, T. *J. Chem. Phys.* **2000**, *113*, 3351.
(30) Kavassalis, T. A.; Sundararajan, P. R. *Macromolecules* **1993**, *26*, 4144. Sundararajan, P. R.; Kavassalis, T. A. *J. Chem. Soc., Faraday Trans.* **1995**, *91*, 2541.
(31) Liao, Q.; Jin, X. *J. Chem. Phys.* **1999**, *110*, 8835.
(32) Muthukumar, M.; Welch, P. *Polymer* **2000**, *41*, 8833.
(33) Fujiwara, S.; Sato, T. *J. Chem. Phys.* **2001**, *114*, 6455.
(34) Liu, C.; Muthukumar, M. *J. Chem. Phys.* **1998**, *109*, 2536.
(35) Meyer, H.; Müller-Plathe, F. *J. Chem. Phys.* **2001**, *115*, 7807.
(36) Meyer, H.; Müller-Plathe, F., manuscript in preparation.
(37) Reith, D.; Meyer, H.; Müller-Plathe, F. *Macromolecules* **2001**, *34*, 2335.
(38) Kremer, K.; Grest, G. S. *J. Chem. Phys.* **1990**, *92*, 5057.
(39) Allen, M.; Tildesley, D. *Computer Simulation of Liquids*; Oxford Science: Oxford, 1987.
(40) Berendsen, H. J. C.; Postma, J. P. M.; van Gunsteren, W. F.; DiNola, A.; Haak, J. R. *J. Chem. Phys.* **1984**, *81*, 3684.
(41) According to the classical theories,[5] s should be close to an equilibrium values: $s = A/\Delta T + \delta s$. These theories were initially designed to describe crystallization from solution. Many works indicate that the underlying assumptions often do not apply; see e.g. refs 6, 9, and 25.

MA011309L